Design of Power System Stabilizer for DFIG-based Wind Energy Integrated Power Systems Under Combined Influence of PLL and Virtual Inertia Controller

Balakrushna Sahu, *Graduate Student Member*, *IEEE* and Bibhu Prasad Padhy, *Member*, *IEEE*

***Abstract*—Wind energy systems (WESs) based on doubly-fed induction generators (DFIGs) have enormous potential for meeting the future demands related to clean energy. Due to the low inertia and intermittency of power injection, a WES is equipped with a virtual inertial controller (VIC) to support the system during a frequency deviation event. The frequency deviation measured by a phase locked loop (PLL) installed on a point of common coupling (PCC) bus is the input signal to the VIC. However, a VIC with an improper inertial gain could deteriorate the damping of the power system, which may lead to instability. To address this issue, a mathematical formulation for calculating the synchronizing and damping torque coefficients of a WES-integrated single-machine infinite bus (SMIB) system while considering PLL and VIC dynamics is proposed in this paper. In addition, a power system stabilizer (PSS) is designed for wind energy integrated power systems to enhance electromechanical oscillation damping. A small-signal stability assessment is performed using the infinite bus connected to a synchronous generator of higher-order dynamics integrated with a VIC-equipped WES. Finally, the performance and robustness of the proposed PSS is demonstrated through time-domain simulation in SMIB and nine-bus test systems integrated with WES under several case studies.**

***Index Terms*—Doubly-fed induction generator (DFIG), virtual inertia controller (VIC), phase locked loop (PLL), small-signal analysis, synchronizing/damping torque, synchronous generator, power system stabilizer (PSS).**

I. Introduction

BECAUSE of their clean, sustainable, and excellent operational characteristics, the integration of wind energy systems (WESs) in power systems has been rapidly increasing [1]. However, the stochastic nature and intermittency of WES behavior pose many challenges to the secure, reliable, and stable operation of power systems. Several researchers have recently conducted systematic investigations of the dynamic interaction of doubly-fed induction generators (DFIGs) and synchronous generators (SGs) of power systems on an electromechanical time scale [2]-[4]. The effects of WES dynamics on electromechanical oscillatory modes (EmOMs) of power systems are demonstrated in [2]. References [2] and [5] conclude that DFIG-based wind farms are practically decoupled from power systems, which minimally affects low-frequency EmOMs. However, DFIGs with improper phase locked loop (PLL) settings may deteriorate the small-signal stability of power systems [4], [6]. According to [7], a high penetration level of type 3/4 wind power generation without a frequency control capacity may result in decreased frequency response tendencies on the power system due to a low-inertia system. Thus, a WES that uses frequency support technology is critical for enhancing the stability and security of power systems. Previous studies have shown that the frequency control scheme of a WES is accomplished through two methods: frequency droop control and virtual inertia control (VIC) [8]. Many researchers have determined that VIC can provide inertial support with improved system frequency regulation (SFR). The frequency support can be provided by injecting active power [9] or extracting kinetic energy stored in the wind farm [10]. One significant advantage of extracting kinetic energy for frequency stability is that the wind generator does not need to deviate from the maximal power point tracking (MPPT) during normal operation (i.e., the derated operation is avoided), and results in reduced energy waste [11]. According to [12], increased wind penetration can adversely affect low-frequency EmOMs. Furthermore, [12] concludes that the inertial response from the WES protects the system from stability loss and improves damping of inter-area system modes. A key performance indicator is proposed in [13] to understand the frequency stability limit of wind generators in power system planning studies. Under severe contingency conditions, extraction of kinetic energy by conventional VIC reduces the efficiency of variable-speed wind generators. This issue has been resolved by proposing an adaptive VIC [14].

Reference [15] proposes an adaptive virtual capacitor to provide inertial support. Later, [16] develops an optimal auxiliary frequency controller containing only a droop controller

Manuscript received: March 31, 2023; revised: May 25, 2023; accepted: June 9, 2023. Date of CrossCheck: June 9, 2023. Date of online publication: July 3, 2023.

B. Sahu (corresponding author) and B. P. Padhy are with Department of Electrical Engineering, Indian Institute of Technology Ropar, Punjab, 140001, India (e-mail: 2018eez0005@iitrpr.ac.in; bibhu@iitrpr.ac.in).

DOI: 10.35833/MPCE.2023.000202

for wind turbine governors (WTGs) operating at MPPT for improved SFR. As part of the work in [17], the kinetic energy from an SG and locally installed DFIG is shared to improve the transient and dynamic stability of the power system. In [18], an optimized proportional-integral-derivative controller is proposed to improve the performance of VIC to achieve better frequency stability. References [19] and [20] investigate power system stability in terms of energy dissipation under the combined influence of a PLL and VIC. The studies have found that with a higher virtual inertial gain, the possibility that the energy dissipation may cause power system instability will be greater. Reference [20] explicitly shows that a WES with a PLL and VIC participates significantly in the low-frequency EmOMs of the power system. Therefore, careful cooperation in the design of the PLL is required for wind power system that includes a PLL and VIC, as improved power angle stability in the power system can then be achieved.

Briefly, a survey of the existing literature reveals the acceptable positive impact of VIC on power system stability. The VIC uses a local-frequency phase angle as input to control the active power output of the WES [21]. It also utilizes a PLL to measure the local frequency. The literature review also reveals that few studies have conducted thorough analyses of the effects of DFIG-based WES on the electromechanical dynamics of power systems. Therefore, research on power system stability under the combined influence of PLL and VIC has adequate scope. The main goal of this paper is to establish a correlation between the electromechanical oscillation dynamics of the SG and the effects of DFIG-based wind energy integration on the power system. The paper investigates the effects of DFIG integration on the electromechanical oscillation dynamics of the SG under the combined influence of a PLL and VIC. In addition, this paper demonstrates the manner in which a retuned power system stabilizer (PSS) of an SG under the influence of PLL and VIC dynamics of a DFIG improves the electromechanical oscillatory characteristics of the power system. These objectives are achieved by developing mathematical functions for a single-machine infinite bus (SMIB) system integrated with DFIG-based WES that defines the electromechanical dynamics of the SG. To the best of our knowledge, this analysis of DFIG-based wind energy integrated power systems under the combined influence of PLL and VIC is a novel study. The contributions of this paper in addressing the aforementioned research gaps are as follows.

1) A mathematical formulation is developed based on the effects of the VIC of a DFIG-based wind farm on the electromechanical dynamics of the power system under PLL influence. As part of the formulation, the joint effect of the VIC and PLL are incorporated by retaining the original Heffron-Phillips model.

2) Based on the modified Heffron-Phillips model, a PSS for SMIB is designed with parameters tuned to consider the effects of the VIC and PLL of a DFIG-based wind farm.

3) The effects of the VIC and PLL on the EmOM is characterized in terms of changes to synchronizing and damping torque coefficients, which are functions of VIC and PLL parameters.

4) Finally, a systematic analysis is conducted to explore the expression of change in synchronizing and damping torque coefficients with respect to increased proportional gains of the VIC. A time-domain simulation of a VIC-installed WES integrated with a single machine system and IEEE 9-bus system is conducted to validate the theoretical foundation.

The remainder of this paper is organized as follows. Section II describes the modeling of the DFIG-based wind energy integrated power system. The dynamic modeling of an SMIB with a DFIG-based WES is presented in Section III. Section IV proposes a design algorithm for the proposed PSS. Section V describes how the exclusive expression of change in the synchronizing/damping torque as a function of VIC and PLL parameters is conducted. Results and discussion related to a technical understanding of the derived expression are presented in Section VI. Finally, a conclusion is given in Section VII.

II. Modeling of DFIG-based Wind Energy Integrated Power System

Our analysis consists of a SMIB system integrated with DFIG-based WES. Figure 1 presents a schematic of a modified SMIB system where the variables are defined in the following text. In this paper, the DFIG-based WES is modeled by aggregating multiple DFIGs with the same capacity and operating state connected in parallel to a single generator. The complete system associated with a DFIG-based WES is basically classified into three categories: mechanical system, induction generator, and converters with controllers. In Fig. 1, P_{opt} is the MPPT power output of DFIG-based WES.

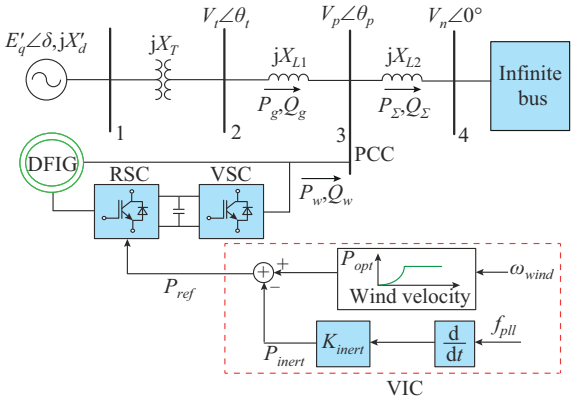

Fig. 1. Modified SMIB system.

A. Modeling of a Mechanical System

A single-mass drive-rotational system models the mechanical part of the overall power system. The mechanical system provides the input power to the wind system based on wind velocity. The shaft torque, i.e., the input to the wind turbine, is defined by:

$$T_{shD} = \sum_{i=1}^{n} \frac{1}{2} B\omega_s C_p^i \frac{(V_w^i)^3}{\omega_{rD}} \tag{1}$$

where B, C_p^i, ω_{rD}, ω_s, and V_w^i are the torque parameter, pow-

er coefficient of the wind turbine, rotor angular velocity of the DFIG, rotor angular velocity of the SG, and wind velocity, respectively. The dynamics of the single-mass model of the rotational system can be defined as:

$$\frac{\mathrm{d}\omega_{rD}}{\mathrm{d}t} = \frac{\omega_s}{2H_D}(T_{shD} - T_{eD}) \tag{2}$$

where H_D is the inertial constant of the wind turbine generator (WTG); and T_{eD} is the electromagnetic torque of the DFIG, which is given by:

$$T_{eD} = E'_{Dd} I_{Dds} + E'_{Dq} I_{Dqs} \tag{3}$$

where $E'_{Dq} - \mathrm{j}E'_{Dd}$ and $I_{Dqs} - \mathrm{j}I_{Dds}$ are the rotor-induced electromagnetic field (EMF) and stator current of the DFIG in the *d-q* axis, respectively.

B. Modeling of DFIGs

DFIGs are used for electricity generation from available wind power. The rotor flux dynamics are used to simulate the DFIG under the assumption that the stator flux linkage is infinitely fast. The dynamics of internal-induced EMF in the *d-q* axis of DFIG can be expressed as:

$$\frac{\mathrm{d}E'_{Dd}}{\mathrm{d}t} = \frac{1}{T'_o}[(X_s' - X_s)I_{Dds} - E'_{Dq}] + (\omega_{rD} - \omega_s)E'_{Dd} + \frac{X_m}{X_r}\omega_s V_{Ddr} \tag{4}$$

$$\frac{\mathrm{d}E'_{Dq}}{\mathrm{d}t} = \frac{1}{T'_o}[(X_s - X_s')I_{Dqs} - E'_{Dd}] - (\omega_{rD} - \omega_s)E'_{Dq} - \frac{X_m}{X_r}\omega_s V_{Dqr} \tag{5}$$

where T'_o, X_s, X'_s, X_r, and X_m are the open-circuit transient time constant, stator reactance, stator transient reactance, rotor reactance, and mutual reactance of the stator and rotor of a DFIG, respectively; and $V_{Dqr} - \mathrm{j}V_{Ddr}$ is the *d-q* axis rotor voltage of the DFIG in the complex form.

C. Modeling of Controllers Associated with Converters

The converters at the rotor and grid sides are known as the rotor-side converter (RSC) and grid-side converter (GSC), respectively. The GSC in this paper is modeled as a constant current source. The transient behaviors of the active and reactive power controllers of the RSC are expressed as:

$$\begin{cases} \dfrac{\mathrm{d}x_1}{\mathrm{d}t} = K_{i1}(P_{ref} - P_{gen}) \\ \dfrac{\mathrm{d}x_2}{\mathrm{d}t} = K_{i2}[K_{p1}(P_{ref} - P_{gen}) + x_1 - I_{Dqr}] \\ \dfrac{\mathrm{d}x_3}{\mathrm{d}t} = K_{i3}(Q_{ref} - Q_{gen}) \\ \dfrac{\mathrm{d}x_4}{\mathrm{d}t} = K_{i4}[K_{p3}(Q_{ref} - Q_{gen}) + x_3 - I_{Ddr}] \end{cases} \tag{6}$$

where $P_{ref} - \mathrm{j}Q_{ref}$ and $P_{gen} - \mathrm{j}Q_{gen}$ are the reference and generated power outputs of the DFIG, respectively; $K_{px} + K_{ix}/s$ ($x = 1, 2, 3, 4$) denotes the PI controllers associated with the RSC; x_1, x_2, x_3, and x_4 are the state variables associated with RSC controllers; and $I_{Dqr} - \mathrm{j}I_{Ddr}$ is the *d-q* axis rotor current of the DFIG in the complex form. Based on the assumption that the wind velocity is within its limit, the transient of the pitch angle controller is not included here. This paper conducts stability analysis for a DFIG-based wind energy integrated power system using a PLL for grid synchronization and VIC to provide inertial support during frequency deviation events. The following equations describe the transient behavior of the PLL:

$$\frac{\mathrm{d}x_{pll}}{\mathrm{d}t} = K_i^{pll} V_p(\theta_p - \theta_{pll}) \tag{7}$$

$$\frac{\mathrm{d}\theta_{pll}}{\mathrm{d}t} = K_p^{pll} V_p(\theta_p - \theta_{pll}) + x_{pll} \tag{8}$$

where $V_p \angle \theta_{pll}$ is the voltage at PCC; θ_p is the voltage angle of the point of common coupling (PCC) bus; $K_p^{pll} + K_i^{pll}/s$ denotes the PI controller used in PLL; and x_{pll} is the intermediate state variable related to PI of PLL. The transient of the VIC is modeled by:

$$\frac{\mathrm{d}x_{vic}}{\mathrm{d}t} = \frac{1}{T}(f_{pll} - x_{vic}) \tag{9}$$

where f_{pll}, x_{vic}, and T are the PLL output frequency, associated state variable, and time constant of the VIC, respectively. Based on (2) - (9), the transient equivalent model of the DFIG-based wind power system can be represented by:

$$\dot{\boldsymbol{x}}_w(t) = \boldsymbol{w}(t) \tag{10}$$

where $\boldsymbol{x}_w(t) = [\omega_{rD}, E'_{Dd}, E'_{Dq}, x_1, x_2, x_3, x_4, x_{pll}, \theta_{pll}, x_{vic}]$; and $\boldsymbol{w}(t)$ is the rector of functions of the first derivative of state variables. In this manner, the 10-order model of the DFIG is integrated into the power system, where the power system in this paper is composed of 4-order SGs. The following state equations define the small-signal equivalent model of the open loop of the power system and the DFIG-based WES:

$$\begin{cases} \Delta\dot{\boldsymbol{x}}_s = \boldsymbol{A}_s\Delta\boldsymbol{x}_s + \boldsymbol{B}_s\Delta\boldsymbol{P}_w \\ \Delta\boldsymbol{V}_P = \boldsymbol{C}_s\Delta\boldsymbol{x}_s + \boldsymbol{D}_s\Delta\boldsymbol{P}_w \end{cases} \tag{11}$$

$$\begin{cases} \Delta\dot{\boldsymbol{x}}_w = \boldsymbol{A}_w\Delta\boldsymbol{x}_w + \boldsymbol{B}_w\Delta\boldsymbol{V}_P \\ \Delta\boldsymbol{P}_w = \boldsymbol{C}_w\Delta\boldsymbol{x}_w + \boldsymbol{D}_w\Delta\boldsymbol{V}_P \end{cases} \tag{12}$$

where $\boldsymbol{x}_s$ is the state vector of n SGs of the power system, $\boldsymbol{x}_s = [\delta, \omega, E'_q, E_{fd}]^{\mathrm{T}}_{7\times n}$, and the state variables δ, ω, E'_q, and E_{fd} are the load angle, angular velocity, transient internal EMF, and exciter field voltage, respectively; $\boldsymbol{P}_w$ and $\boldsymbol{V}_P$ are the injected power and voltage matrices at the PCC of the DFIG, respectively; $\boldsymbol{A}_s$, $\boldsymbol{B}_s$, $\boldsymbol{C}_s$, and $\boldsymbol{D}_s$ are the state matrix, input matrix, output matrix, and feedforward matrix, respectively; and $\boldsymbol{A}_w$, $\boldsymbol{B}_w$, $\boldsymbol{C}_w$, and $\boldsymbol{D}_w$ are defined in the similar fashion as of $\boldsymbol{A}_s$, $\boldsymbol{B}_s$, $\boldsymbol{C}_s$, and $\boldsymbol{D}_s$. From (11) and (12), the state equation of the entire system takes the following form:

$$\dot{\boldsymbol{x}} = \boldsymbol{A}_{sys}\boldsymbol{x} \tag{13}$$

where $\boldsymbol{x} = [\boldsymbol{x}_s, \boldsymbol{x}_w]^{\mathrm{T}}$; and $\boldsymbol{A}_{sys}$ is the closed loop system state matrix. The following assumptions are adopted in the subsequent sections to investigate the effects of the DFIG-based WES on the power system under the influence of VIC and PLL dynamics.

1) A single-mass drive-train system models the mechanical part of the wind turbine.

2) The turbine pitch angle controller is not modeled.

3) The GSC is modeled as a controlled current source.

4) All analysis is conducted on the assumption of a constant wind velocity, where the wind velocity is assumed to be within the operational limit.

5) The nominal frequency of the entire system is 60 Hz.

III. Dynamic Modeling of an SMIB with a DFIG-based WES

A DFIG-based WES endowed with a VIC can support power system frequency by changing the reference current of the RSC controller [20]. The VIC is installed near the RSC of the DFIG. As Fig. 1 shows, the change in system frequency is measured by the PLL of the DFIG and processed through the VIC as a positive frequency error, which is then transformed into a corresponding inertial power output of VIC (P_{inert}). Thus, in frequency excursion events, P_{inert} alters the reference of the RSC active power controller to extract stored kinetic energy of the rotor. The VIC controller with an improper gain setting can adversely affect the system. Therefore, it is essential to investigate the exact impact of the VIC on the small-signal stability of the power system. This section describes the theoretical basis for small-signal stability analysis of an SMIB system integrated with a DFIG-based WES. The theoretical study interprets the manner in which the dynamics of a PLL and VIC of a WES affect the electromechanical modes of the SG. As Fig. 1 shows, an SG is installed at Bus 1, and the DFIG is installed at Bus 3. Buses 1 and 3 are connected through a transformer and lossless transmission line. The SG is modeled as a third-order flux decay model [22]. The differential equations associated with SGs and exciter dynamics [22] are given as:

$$\begin{cases} \dot{\delta} = \omega - \omega_s \\ \dot{\omega} = \dfrac{\omega_s}{2H}(P_m - P_g) \\ \dot{E}'_q = \dfrac{1}{T'_{do}}[E_{fd} - E'_q - (X_d - X'_d)I_d] \\ \dot{E}_{fd} = \dfrac{1}{T_A}[-E_{fd} + K_A(V_{ref} - V_t)] \end{cases} \tag{14}$$

The variables and parameters of (14) follow the standardized notations from [22]. In the absence of a WES, the power balance equation at Bus 3 satisfies:

$$\begin{cases} P_\Sigma = P_g \\ Q_\Sigma = Q_g \end{cases} \tag{15}$$

where $P_g = \dfrac{E'_q V_p}{X_{L1} + X_T + X'_d}\sin(\delta - \theta_p)$, $P_\Sigma = \dfrac{V_p V_n}{X_{L2}}\sin\theta_p$, $Q_g = \dfrac{E'_q V_p \cos(\delta - \theta_p)}{X_{L1} + X_T + X'_d} - \dfrac{V_p^2}{X_{L1} + X_T + X'_d}$, $Q_\Sigma = \dfrac{V_p^2}{X_{L2}} - \dfrac{V_p V_n}{X_{L2}}\cos\theta_p$, $V_p\angle\theta_p$ and $V_n\angle 0°$ are the bus voltages of the PCC and infinite bus, respectively, X_d and X'_d are the d-axis steady-state and transient reactance of the SG, respectively, δ is the internal bus voltage angle of the SG given in Fig. 1, and X_{L1}, X_{L2}, and X_T are the reactances of the transmission lines $L1$, $L2$, and transformer, respectively, which are considered to be lossless. Thus, the line and transformer equivalent impedances have only imaginary parts. Linear modal analysis is conducted by linearizing the nonlinear differential-algebraic equations of the power system given in (14) and (15). In small-signal stability analysis, the change in electrical power output following a perturbation can be resolved into two components, namely, synchronizing and damping power. Hence,

$$\Delta P_g = P_S \Delta\delta + P_D \Delta\omega \tag{16}$$

where P_S and P_D are the synchronizing and damping coefficients, respectively. The coefficients can be evaluated for an electromechanical mode of interest (EMI) $\bar{\lambda}_c$ and are widely used to measure the small-signal stability of power systems [23]. This section describes how the modified Heffron-Phillips model is evaluated under the joint VIC-PLL effect for EMI $\bar{\lambda}_c$. To incorporate the effects of the WES, the power balance expressed in (15) can be augmented to:

$$P_\Sigma = P_g + P_w \tag{17}$$

The linear form of (17) can be expressed as:

$$\Delta P_\Sigma = \Delta P_g + \Delta P_w \tag{18}$$

where $\Delta P_\Sigma = \left(\dfrac{V_{p0}V_{n0}}{X_{L2}}\cos\theta_{p0}\right)\Delta\theta_p + \dfrac{P_{g0}}{V_{p0}}\Delta V_p$; and $\Delta P_g = \left(\dfrac{E'_{q0}V_{p0}}{X_1}\cos(\delta_0 - \theta_{p0})\right)(\Delta\delta - \Delta\theta_p) + P_{g0}\left(\dfrac{1}{E'_{q0}}\Delta E'_q + \dfrac{1}{V_{p0}}\Delta V_p\right)$, in which X_1 is defined as $X_1 = X_{L1} + X_T + X'_d$. The variables with subscript "0" indicate the initial operating points. Based on [4] and [24], the DFIG-based WES without VIC is practically decoupled from the rest of the power system (i.e., the rotor velocity is decoupled with grid frequency). Therefore, the DFIG active power output P_w does not vary with small disturbance at the grid side. However, a DFIG endowed with VIC can modulate P_w with a frequency variation. The frequency variation at the PCC is measured by the PLL. Thus, P_w variation with the VIC and PLL can be defined as:

$$\Delta P_w = \begin{cases} -sK_{inert}\Delta f_{pll} & \text{with VIC and PLL} \\ 0 & \text{without VIC} \end{cases} \tag{19}$$

where K_{inert} and f_{pll} are the proportional gain of the VIC and the frequency at the PCC measured by the PLL, respectively. The model of PLL based on a synchronously-rotating-reference frame (SRF-PLL) considered in this paper is shown in Fig. 2. Based on the assumption that $V_p = 1$ p.u., the relationship between Δf_{pll} and $\Delta\theta_p$ can be expressed as:

$$\Delta f_{pll} = \frac{s}{2\pi}\frac{sK_{P,pll} + K_{I,pll}}{s^2 + sK_{P,pll} + K_{I,pll}}\Delta\theta_p \tag{20}$$

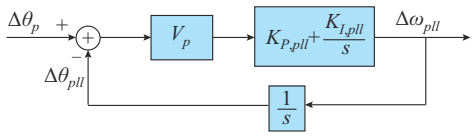

Fig. 2. Model of SRF-PLL.

Thus, with the PI parameters of the PLL (i.e., $K_{P,pll}$ and $K_{I,pll}$), (19) can be rewritten as:

$$\Delta P_w = \begin{cases} -s^2\dfrac{K_{inert}}{2\pi}\dfrac{sK_{P,pll} + K_{I,pll}}{s^2 + sK_{P,pll} + K_{I,pll}}\Delta\theta_p & \text{with use of VIC and PLL} \\ 0 & \text{without use of VIC} \end{cases} \tag{21}$$

Next, to consider the contribution of wind power controllers, the change in wind energy active power output can be expressed as:

$$\Delta P_w = -s^2 \frac{K_{inert}}{2\pi} F_{pll}(s) \Delta\theta_p \tag{22}$$

where $F_{pll}(s)$ is the transfer function of PLL referred from (20) and (21). Similarly, the reactive power balance of (15) is linearized to obtain the expression of ΔV_p. Based on the assumption that the DFIG reactive power output $Q_w = 0$, the linearization of the reactive power balance of (15) becomes:

$$\Delta Q_g - \Delta Q_\Sigma = 0 \tag{23}$$

$$\begin{cases} \Delta Q_\Sigma = \dfrac{V_p}{X_{L2}} \Delta V_p + \dfrac{Q_{\Sigma 0}}{V_{p0}} \Delta V_p + P_{\Sigma 0} \Delta\theta_p \\ \Delta Q_g = \dfrac{V_{p0}}{X_1} \cos(\delta_0 - \theta_{p0}) \Delta E'_q - P_{g0} (\Delta\delta - \Delta\theta_p) + \left(\dfrac{Q_{g0}}{V_{p0}} - \dfrac{V_{p0}}{X_1} \right) \Delta V_p \end{cases} \tag{24}$$

A modified Heffron-Phillips model can then be obtained by linearizing the nonlinear dynamics of the power system defined in (14)-(23) at an operating point when considering the dynamics of a WES endowed with VIC. The additional contribution to the original K_1-K_6 constants of the SMIB can be obtained, respectively, as:

$$\begin{cases} \Delta K_1 = \dfrac{X_{L2} (E'_{q0})^2 V_{p0} \cos^2(\delta_0 - \theta_{p0})}{X_1 M_{en}} D(s) \\ \Delta K_2 = -\dfrac{P_{g0} X_{L2} \cos(\delta_0 - \theta_{p0})}{X_1 M_{en}} D(s) \\ \dfrac{1}{\Delta K_3} = \dfrac{P_{g0}^2 (X_d - X'_d) X_1 X_{L2}}{V_{p0} M_{en}} D(s) \\ \Delta K_4 = \dfrac{P_{g0} (X_d - X'_d) \cos(\delta_0 - \theta_{p0}) X_{L2}}{M_{en}} D(s) \\ \Delta K_5 = \dfrac{X_{L1} X_{L2} P_{g0}}{M_{ep}} D(s) \\ \Delta K_6 = -\dfrac{P_{g0}^2 X_{L1} X_{L2} X_1 X'_d}{E'_q V_{P0} M_{en} M_{ep}} D(s) \end{cases} \tag{25}$$

where $D(s) = \dfrac{s^2 \dfrac{K_{inert}}{2\pi} F_{pll}(s)}{\dfrac{V_{p0}}{X_1 X_{L2}} M_{en} + s^2 \dfrac{K_{inert}}{2\pi} F_{pll}(s)}$; $M_{en} = V_{n0} X_1 \cos\theta_{p0} + E'_{q0} X_{L2} \cos(\delta_0 - \theta_{p0})$; and $M_{ep} = E'_{q0} X_{L1} \cos(\delta_0 - \theta_{t0}) + V_{p0} X'_d \cos(\theta_{t0} - \theta_{p0})$.

The steps for deriving the aforementioned functions are presented in Appendix A. The modified K_1-K_6 are then transformed into:

$$\begin{cases} G_i(s) = K_i + \Delta K_i(s) & i = 1, 2, 4, 5, 6 \\ \dfrac{1}{G_i(s)} = \dfrac{1}{K_i} + \dfrac{1}{\Delta K_i(s)} & i = 3 \end{cases} \tag{26}$$

All $G_i(s)$ retain the properties of the classical Heffron-Phillips model, as shown in Fig. 3. The following section describes how the properties of the automatic voltage regulator (AVR) and PSS are used for further analysis.

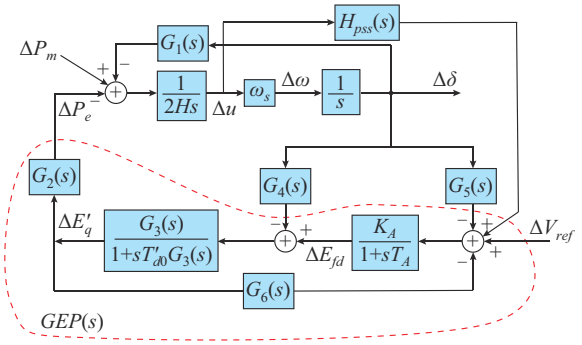

Fig. 3. Structure of classical Heffron-Phillip model with inertia controller and PLL dynamics of wind power controller.

IV. Design Algorithm for Proposed PSS

The design of a PSS for the SG when considering the effects of the VIC and PLL dynamics of the DFIG can improve the system's damping properties. Instead of those of the conventional PSS (CPSS), the parameters of the proposed PSS are derived from the modified Heffron-Phillips model that incorporates the VIC and PLL dynamics of the DFIG. However, the structure of the transfer function model is identical to that of the CPSS. Thus, no limitation exists for the proposed PSS from a mathematical or implementation standpoint. The most efficient design of the PSS is by means of the transfer function of $GEP(s)$, where $GEP(s)$ represents the transfer function between the change in electrical power output and the reference voltage, as shown in Fig. 3 and expressed as:

$$GEP(s) = \frac{-G_2(s) G_3(s) H_{EXC}(s)}{G_3(s) G_6(s) H_{EXC}(s) + 1 + s G_3(s) T'_{d0}} \tag{27}$$

where $H_{EXC}(s)$ is the transfer function of the exciter dynamics, which is a lead-lag type of compensator preferable for being used as the model of the PSS, as expressed in (28). This lead-lag compensator provides a sufficient phase lead to compensate for the phase lag of the feedback loop at a low-frequency EmOM.

$$H_{pss}(s) = K_{pss} \frac{s T_w}{1 + s T_w} \frac{1 + s T_1}{1 + s T_2} \frac{1 + s T_3}{1 + s T_4} \tag{28}$$

All the parameters of the PSS as given in (28) accord with the standard notations in [22]. The tuning steps of the proposed PSS parameters referenced in Algorithm 1 ensure sufficient damping for the critical EmOM. The difference between the tuning guidelines mentioned in [25] and those outlined in Algorithm 1 is that instead of constant parameters for the Heffron-Phillips model, here we use $G_1(s)$-$G_6(s)$.

Power electronic converters control nearly 30% of the total electric power generation from DFIG-based wind technology. The rest of the power is directly fed to the grid through the DFIG stator, which is controlled by a mechanically rotated wind turbine. During electrical faults, the mechanical power available at the input of DFIG is more than the electrical power available at its terminal. Thus, during a fault, when a frequency event is triggered, the application of the proposed PSS design method with a proper setting of VIC gain K_{inert} as demonstrated in this paper can stabilize the system by extracting kinetic energy stored in the rotor of the

DFIG. Therefore, even if no energy storage device is installed in the system, the drive-train will not be placed under additional strain.

Algorithm 1: tuning steps of proposed PSS parameters

Input: all data related to SG, VIC, and PLL

1: Obtain K_1-K_6 from the classical Heffron-Phillips model

2: Obtain the functions of $G_1(s)$-$G_6(s)$ from the modified Heffron-Phillips model using (26) and Appendix A

3: Neglecting damping from all other sources, obtain undamped natural frequency (ω_n) from torque angle loop presented in Fig. 3

4: Obtain the phase lag of $GEP(s)$ of (27) at $s=\mathrm{j}\omega_n$

5: Set the phase lead of $H_{pss}(s)$ in (28) such that $\angle H_{pss}(s)|_{s=\mathrm{j}\omega_n}+\angle GEP(s)|_{s=\mathrm{j}\omega_n}=0$

6: Obtain the instability PSS gain K_{pss}^c from the root locus plot of the system, including PSS, and then set $K_{pss}=K_{pss}^c/3$

Output: proposed PSS parameters

V. Effects of VIC and PLL of WES on Changes to System Synchronizing/Damping Torque

To assess the dynamic effects of the DFIG on the damping of the SG, we next determine the ΔP_g in terms of $\Delta\delta$ and $\Delta\omega$ as a function of the VIC and PLL parameters. This can be accomplished by further constructing $\Delta E_q'$ in terms of $\Delta\delta$ and $\Delta\omega$. The relationship of $\Delta E_q'$ to $\Delta\delta$ and $\Delta\omega$ can be evaluated in a similar manner as in [26] and represented as:

$$\Delta E_q'(s)=\Lambda_{avr}(s)\Delta\delta+\Lambda_{pss}(s)\Delta\omega \tag{29}$$

$$\begin{cases}\Lambda_{avr}(s)=\dfrac{-(G_4(s)+G_5(s)H_{EXC}(s))G_3(s)}{G_3(s)G_6(s)H_{EXC}(s)+1+sG_3(s)T_{d0}'}\\ \Lambda_{pss}(s)=\dfrac{-G_3(s)H_{pss}(s)H_{EXC}(s)}{G_3(s)G_6(s)H_{EXC}(s)+1+sG_3(s)T_{d0}'}\end{cases} \tag{30}$$

Next, if we substitute (29) into (A2) of Appendix A, the change in generator output power can be expressed as:

$$\Delta P_g=(G_1(s)+G_2(s)\Lambda_{avr}(s))\Delta\delta+G_2(s)\Lambda_{pss}(s)\Delta\omega \tag{31}$$

As this paper focuses on low-frequency oscillations less than 3 Hz, we can assume that $G_4(s)$ has a negligible impact on $\Lambda_{avr}(s)$ [27]. With the usual range of generator constants and the tuning process of the AVR and PSS [26], the $\Lambda_{avr}(s)$ and $\Lambda_{pss}(s)$ could be approximated to that of [27] as:

$$\begin{cases}\Lambda_{avr}(s)\approx\dfrac{-G_5(s)}{K_AK_6}\dfrac{H_{exc}(s)}{1+s\dfrac{T_{d0}'}{K_AK_6}}\\ \Lambda_{pss}(s)\approx\dfrac{-H_{exc}(s)H_{pss}(s)}{K_AK_6\left(1+s\dfrac{T_{d0}'}{K_AK_6}\right)}\end{cases} \tag{32}$$

Then, with the replacement of $\Lambda_{avr}(s)$ and $\Lambda_{pss}(s)$ from (32) into (31), ΔP_g for EMI can be expressed in the form of (16) as:

$$\Delta P_g|_{s=\lambda_c+\Delta\lambda_c}=P_S\Delta\delta+P_D\Delta\omega \tag{33}$$

$$P_S=G_1(s)-\frac{G_2(s)G_5(s)H_{EXC}(s)}{K_AK_6\left(1+s\dfrac{T_{d0}'}{K_AK_6}\right)} \tag{34}$$

$$P_D=\frac{-G_2(s)H_{EXC}(s)H_{pss}(s)}{K_AK_6\left(1+s\dfrac{T_{d0}'}{K_AK_6}\right)} \tag{35}$$

where $\Delta\lambda_c$ represents the change in EMI derived from the VIC and PLL dynamics of the DFIG.

From (34) and (35), we can see that the synchronizing/damping coefficients (P_S/P_D) are mostly affected by $G_2(s)$ and $G_5(s)$. Next, we define all the parameters and functions without an inertia controller and PLL, which are marked with "$\hat{}$". With this property, (33) can be rewritten as:

$$\Delta P_g|_{s=\lambda_c+\Delta\lambda_c}=(\hat{P}_S+\Delta P_S)\Delta\delta+(\hat{P}_D+\Delta P_D)\Delta\omega \tag{36}$$

where $\hat{P}_S$ and $\hat{P}_D$ are the synchronizing and damping coefficients for the case without a PLL and VIC, respectively. Thus, for the mode of interest λ_c, $\hat{P}_S$ and $\hat{P}_D$ can be expressed as:

$$\begin{aligned}\hat{P}_S|_{s=\lambda_c}&=K_1+K_2\hat{\Lambda}_{avr}(s)\\ \hat{P}_D|_{s=\lambda_c}&=K_2\hat{\Lambda}_{pss}(s)\end{aligned} \tag{37}$$

where $\hat{\Lambda}_{avr}(s)$ and $\hat{\Lambda}_{pss}(s)$ are the changes in the AVR and PSS transfer functions, respectively. In addition, from (32), the relationship between Λ and $\hat{\Lambda}$ can be described as:

$$\begin{cases}\Lambda_{avr}(s)=\hat{\Lambda}_{avr}(s)\left(1+\dfrac{\Delta K_5(s)}{K_5}\right)\\ \Lambda_{pss}(s)=\hat{\Lambda}_{pss}(s)\end{cases} \tag{38}$$

When (38) is substituted into (31), ΔP_g can be rewritten as:

$$\begin{aligned}\Delta P_g=&\left[\left(K_1+K_2\hat{\Lambda}_{avr}(s)\right)\Delta\delta+K_2\hat{\Lambda}_{pss}(s)\Delta\omega\right]\left(1+\frac{\Delta K_2(s)}{K_2}\right)+\\ &\left[\left(G_2(s)\frac{X_{L1}M_{en}}{X_1M_{vv}}\hat{\Lambda}_{avr}(s)-K_1\right)\frac{\Delta K_2(s)}{K_2}+\Delta K_1(s)\right]\Delta\delta\end{aligned} \tag{39}$$

where $M_{vv}=V_{n0}X_{L1}\cos\theta_{p0}+V_tX_{L2}\cos(\theta_{t0}-\theta_{p0})$.

As highlighted in [25] and [26], with a high AVR gain, both the AVR and PSS offer constant contributions to the synchronizing/damping coefficients for a small change in eigenvalues (i.e., $\lambda_c\to\lambda_c+\Delta\lambda_c$). With this property, (39) can be expressed as:

$$\Delta P_g|_{s=\lambda_c}\approx\Delta P_g|_{s=\lambda_c+\Delta\lambda_c} \tag{40}$$

Equation (39), therefore, becomes:

$$\Delta P_g|_{s=\lambda_c}=\hat{P}_S\Delta\delta+\hat{P}_D\Delta\omega+(P_{Sa}\Delta\delta+P_{Da}\Delta\omega)\frac{\Delta K_2(s)}{K_2} \tag{41}$$

$$\begin{cases}P_{Sa}=\hat{P}_S+\dfrac{X_{L1}M_{en}}{X_1M_{vv}}P_{s,avr}+\dfrac{E_{q0}'V_P}{X_1}\cos(\delta_0-\theta_{p0})-K_1\\ P_{Da}=\hat{P}_D+\dfrac{X_{L1}M_{en}}{X_1M_{vv}}P_{d,avr}\end{cases} \tag{42}$$

The $P_{s,avr}$ and $P_{d,avr}$ are the synchronizing and damping contributions from $K_2\hat{\Lambda}_{avr}(\lambda_c)$, respectively. For the mode of interest, (41) implies that:

$$\Delta P_S\Delta\delta+\Delta P_D\Delta\omega=(P_{Sa}\Delta\delta+P_{Da}\Delta\omega)\frac{\Delta K_2(\lambda_c)}{K_2} \tag{43}$$

Based on (25) and (26), the following is derived:

$$\frac{\Delta K_2(s)}{K_2}=\frac{E'_{q0}X_{L2}\cos(\delta_0-\theta_{p0})}{M_{en}}D(s) \tag{44}$$

Thus, in the mode of interest ($\lambda_c=\sigma_c+\mathrm{j}\omega_c$), the $D(s)$ of (44) can be expressed as:

$$D(s)|_{s=\lambda_c}=D_R+\mathrm{j}D_I \tag{45}$$

If we assume that $\sigma_c \ll \omega_c$ such that $\lambda_c \approx \mathrm{j}\omega_c$, the exclusive expressions of D_R and D_I are:

$$\begin{cases} D_R=\dfrac{-K_{inert}K_{I,pll}\omega_c^2A-K_{inert}K_{I,pll}\omega_c^3B}{A^2+B^2} \\ D_I=\dfrac{K_{inert}K_{I,pll}\omega_c^2B-K_{inert}K_{I,pll}\omega_c^3A}{A^2+B^2} \end{cases} \tag{46}$$

where A and B are expanded to:

$$\begin{cases} A=\dfrac{2\pi V_{p0}M_{en}}{X_1X_{L2}}(K_{I,pll}-\omega_c^2)-K_{inert}K_{I,pll}\omega_c^2 \\ B=\dfrac{2\pi V_{p0}M_{en}}{X_1X_{L2}}K_{P,pll}\omega_c-K_{inert}K_{p,pll}\omega_c^3 \end{cases} \tag{47}$$

Based on (43)-(45), ΔP_S and ΔP_D can ultimately be represented as in (48).

$$\begin{cases} \Delta P_S=\dfrac{E'_{q0}X_{L2}\cos(\delta_0-\theta_{p0})}{M_{en}(A^2+B^2)}[(P_{da}K_{P,pll}\omega_c^2-P_{sa}K_{I,pll})K_{inert}\omega_c^2A- \\ \qquad (P_{sa}K_{P,pll}+P_{da}K_{I,pll})K_{inert}\omega_c^3B] \\ \Delta P_D=\dfrac{E'_{q0}X_{L2}\cos(\delta_0-\theta_{p0})}{M_{en}(A^2+B^2)}[-(P_{da}K_{I,pll}+P_{sa}K_{P,pll})K_{inert}\omega_c^2A+ \\ \qquad (P_{sa}K_{I,pll}-P_{da}K_{P,pll}\omega_c^2)K_{inert}\omega_cB] \end{cases} \tag{48}$$

Thus, the changes in synchronizing and damping coefficients as derived in (48) are the functions of eigenmode, damping frequency ω_c, the VIC and PLL parameters, and synchronizing/damping coefficients from the no-wind integration case ($\hat{P}_S/\hat{P}_D$). According to (48), as K_{inert} increases to a non-zero value, a shift occurs in the mode of interest (i.e., $\Delta\lambda_c$), and the wind power inertial controller participates in damping and synchronizing torque.

VI. Results and Analysis

A. SMIB System

The outcomes described in the previous section were validated through an SMIB test system, as shown in Fig. 1.

1) Effects of Variations in K_{inert} on ΔP_S and ΔP_D

ΔP_S and ΔP_D were studied under different values of K_{inert}. The ΔP_S and ΔP_D curves inherited from (48) were validated against those obtained from (31), which consisted of exact expressions of AVR and PSS contributions. The parameters of the generator and AVR are presented in Appendix B. The wind farm installed at Bus 3 of the SMIB, as shown in Fig. 1, consisted of 22 DFIGs at a 3.6 MVA rating and were connected in parallel. The wind farm was aggregated into a single DFIG for small-signal analysis. The parameters of the PLL used for synchronization purposes of the DFIG were $K_{P,pll}=0.01$ and $K_{I,pll}=0.1$. The remainder of the data related to the SG, transformer, and DFIG are presented in Appendix B Tables BI and BII. It should be noted that the change in the position of DFIG integration in the SMIB system, as shown in Fig. 1, could result in changes to line reactances X_{L1} and X_{L2}. Equation (48) presents the effects of line reactance on the variations in synchronizing and damping torque of the SG. Under these conditions, the study was conducted with DFIGs installed at: ① Location 1: $X_{L1}=0.05$ p.u., $X_{L2}=0.15$ p.u. with the proposed PSS1; and ② Location 2: $X_{L1}=0.15$ p.u., $X_{L2}=0.05$ p.u. with the proposed PSS2. The effects of the location of the DFIG equipped with a VIC and PLL on the synchronizing and damping torque (ΔP_S and ΔP_D) of the SG were studied. In an analysis of the characteristics of ΔP_S and ΔP_D, λ_c was considered to be the same in both cases. With the same data used at Location 1, the initial operating conditions of the system were $P_{g0}=1$ p.u., $P_{w0}=0.88$ p.u., $V_t=1\angle 0.3398$ p.u., $V_{p0}=0.9887\angle 0.2893$ p.u., and $V_{n0}=1\angle 0$ p.u.. Similarly, the operating conditions of Location 2 were $P_{g0}=1$ p.u., $P_{w0}=0.88$ p.u., $V_t=1\angle 0.2462$ p.u., $V_{p0}=0.9938\angle 0.0947$ p.u., and $V_{n0}=1\angle 0$ p.u.. All p.u. values were based on 100 MVA. The parameters of the proposed PSS1 and PSS2 were tuned according to Algorithm 1 and Table I. The changes of ΔP_S and ΔP_D versus K_{inert} at Locations 1 and 2 are shown in Fig. 4.

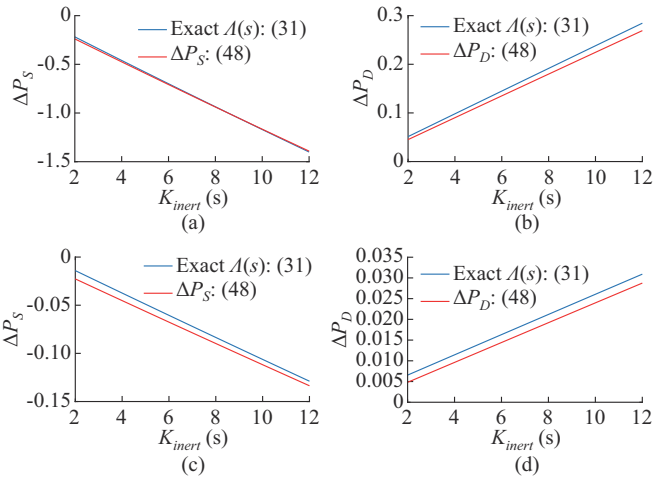

Fig. 4. Changes in ΔP_S and ΔP_D versus K_{inert} at Locations 1 and 2. (a) ΔP_S at Location 1 (proposed PSS1). (b) ΔP_D at Location 1 (proposed PSS1). (c) ΔP_S at Location 2 (proposed PSS2). (d) ΔP_D at Location 2 (proposed PSS2).

TABLE I
PSS Parameters for Locations 1 and 2

PSS	K_{pss}	T_w	T_1	T_2	T_3	T_4
Proposed PSS1	62	10	0.2	0.02	0.1	0.52
Proposed PSS2	40	10	0.2	0.02	0.1	0.64

The degree of mismatch observed in Fig. 4 derives from certain assumptions used to derive (48). Note that the discrepancies in the results as obtained from the approximated expression in (48) and the exact expressions in (29) - (31) could be ignored, as this paper focuses on the nature and properties of the interaction between the wind farm with an inertial controller and the SG. Figure 4 shows that the increase in K_{inert} toward a positive integer adversely affects

ΔP_S such that at a certain value of K_{inert}, the ΔP_S may become negative, which must be avoided to ensure the rotor angle stability of the system. In contrast to ΔP_S, the behavior of ΔP_D increases with K_{inert}. As expected, we conclude from Fig. 4 that the interaction between the wind farm and SG is more prominent when the wind was nearer to the SG, i.e., Location 1, and the effect diminished as it moved to a more remote location, i.e., Location 2.

The aforementioned observations was verified through a time-domain simulation performed in MATLAB 2019b for the system shown in Fig. 1. The SG and AVR parameters used in the simulation are presented in Appendix B. The line parameters were chosen to be the same as for Location 1. A wind farm consisting of 22 DFIGs, each DFIG with power of 3.6 MW, was integrated to the system at Bus 3. Data for each DFIG are provided in Appendix B. The simulation of the inertial loop of the VIC consisted of a rate limiter and low-pass filter to remove the noise from the frequency error signal, which was not modeled for the aforementioned mathematical analysis. This research evaluated the mechanism of power system as derived from DFIG integration while considering VIC and PLL dynamics. More specifically, this paper evaluated the manner in which the DFIG integration into the power system affected the damping and synchronizing torque of the SG. Thus, in this paper, the wind speed was treated as the average of the various wind speeds. Therefore, this paper assumed that the wind velocity and, thus, wind power output were constant. The PLL parameter was set per the value previously mentioned. The PSS parameters were chosen from Table I for Location 1 of the wind farm. Time-domain simulation results of the load angle curve of the system for a three-phase fault applied between the PCC and infinite bus at 1 s were obtained with different values of K_{inert}, as shown in Fig. 5. The system load angle curve was observed for different values of K_{inert}. Figure 5 shows that an increase in K_{inert} may have deteriorated the system rotor angle stability.

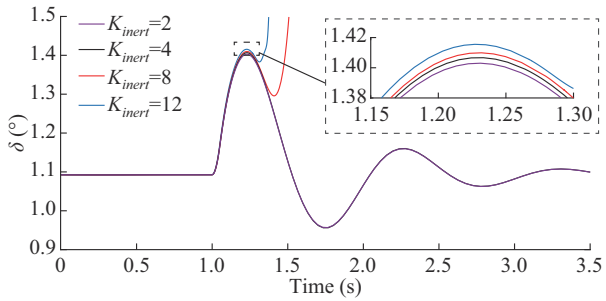

Fig. 5. Dynamic response for different values of K_{inert}.

2) ΔP_S and ΔP_D Versus CPSS and Proposed PSS

To demonstrate the effects of the proposed PSS and CPSS on changes in ΔP_S and ΔP_D, the proposed PSS for Location 1 was designed according to the steps outlined in Algorithm 1. The CPSS parameters were tuned without considering the effects of the VIC and PLL. The modified Heffron-Phillips model was derived for the given location of the wind farm. To design the proposed PSS for the SG, the PSS parameters were assumed to be $T_1 = 0.2$ s, $T_2 = 0.02$ s, and $T_3 = 0.1$ s. T_4 was inferred from the phase-lagging information of $GEP(j\omega_n)$. In this case, the undamped natural frequency was obtained as $\omega_n = 8.03$ Hz, with damping from all other sources neglected. For the given ω_n, T_4 is obtained as 0.52 s. Then, K_{pss} was derived from the root locus diagram considering the dynamics of the full system. The root locus of the SG is presented in Fig. 6. According to the root locus diagram, the critical value of PSS gain $K_{pss}^{cr} = 185$. Thus, in accordance with *Step 4* of Algorithm 1, $K_{pss} = 62$. Figure 7(a) and (b) represents the changes in ΔP_S and ΔP_D with respect to K_{inert} for the proposed PSS and CPSS, respectively. The parameters of the proposed PSS and CPSS are presented in Table II. Figure 7 shows that the proposed PSS significantly improved the damping contribution from wind farms over that of the CPSS with respect to the complete range of K_{inert}. These observations were validated through a time-domain simulation developed in MATLAB 2019b of the given system with $K_{inert} = 4$. A three-phase fault was applied at 1 s between the PCC and infinite bus. The fault response of load angle curve "δ", as shown in Fig. 8, clearly revealed that the proposed PSS exhibited very impressive damping characteristics over those of the CPSS.

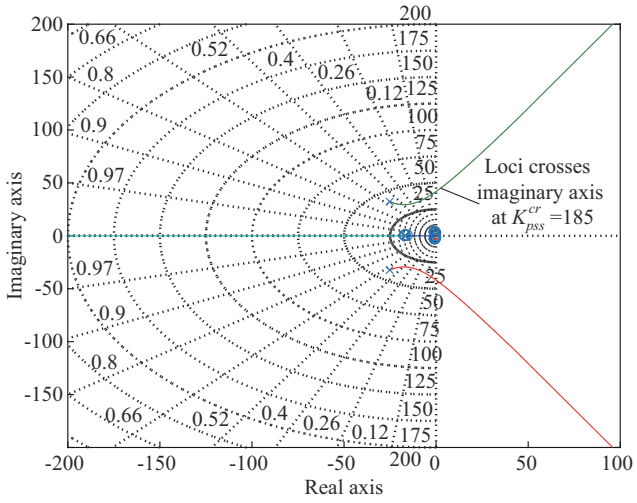

Fig. 6. Root locus of SG.

TABLE II
PARAMETERS OF PROPOSED PSS AND CPSS

Type of PSS	K_{pss}	T_w	T_1	T_2	T_3	T_4
Proposed PSS	62	10	0.2	0.02	0.1	0.53
CPSS	30	10	0.2	0.02	0.1	0.42

The system response under fast dynamic conditions is shown in Figs. 5 and 8 for the SMIB system under the application of a three-phase fault between the PCC and infinite bus. The figures conclusively show that the proposed PSS, which was designed to consider the effects of the VIC and PLL of the DFIG at a lower range of K_{inert}, exhibited impressive results compared with the CPSS. The infinite bus is considered an ideal voltage source with no internal impedance. However, as Fig. 1 shows, the line impedance connected between the PCC bus and infinite bus was X_{L2}. Based on (48), X_{L2} is one of the function parameters of ΔP_S and ΔP_D. The

effects of changes in X_{L2} were simulated by changing the location of the DFIG. Here, X_{L2} could be treated as grid impedance. This research considered the two locational scenarios of Locations 1 and 2. Results under the two locations are presented in Figs. 4-8. From these plots, we concluded that when the DFIG was located near the SG, the interaction between the DFIG and SG was prominent in terms of improved synchronizing and damping torque. Alternatively, high grid impedance promoted better system stability.

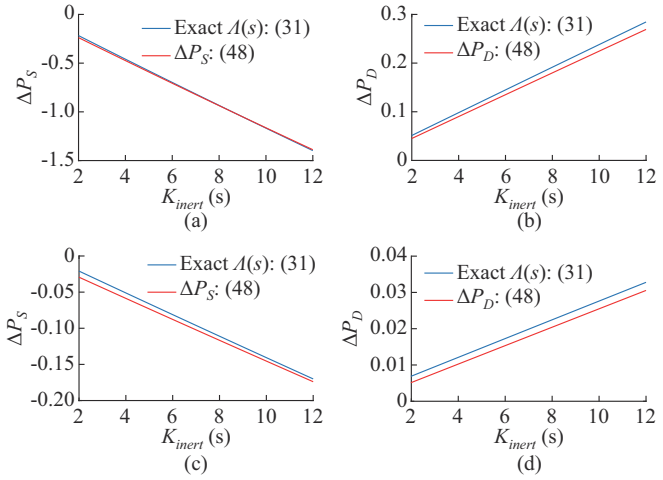

Fig. 7. Change in ΔP_S and ΔP_D versus K_{inert} with proposed PSS and CPSS. (a) ΔP_S with proposed PSS. (b) ΔP_D with proposed PSS. (c) ΔP_S with CPSS. (d) ΔP_D with CPSS.

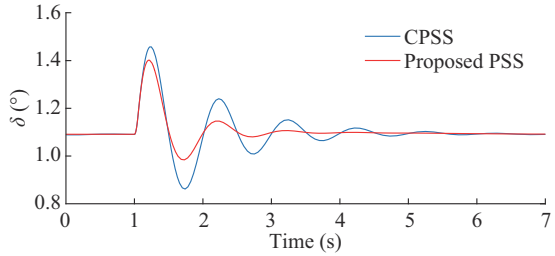

Fig. 8. Simulation result of fault responses of CPSS and proposed PSS.

B. Modified IEEE 9-bus Test System

The modified IEEE 9-bus test system, as shown in Fig. 9, has a wind farm installed at Bus 7. All the parameters for the IEEE 9-bus test system were derived from [22]. A wind farm with 50 DFIG-based wind generators with stator-side capacities of 1.5 MW each is assumed to be installed near generator 2.

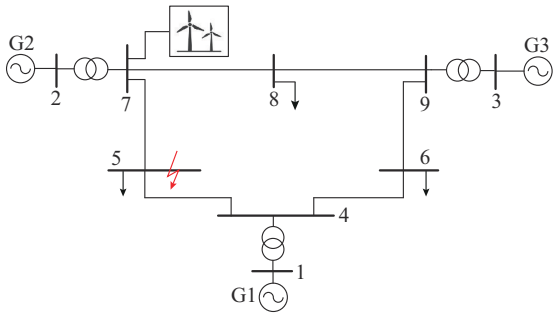

Fig. 9. Modified IEEE 9-bus test system.

1) Effects of Variations in K_{inert}

In this paper, a generator nearest the wind farm was identified for installing the PSS. The PLL of the rotor-side converter was set to be $K_{p,pll}=0.52$ and $K_{i,pll}=17$. The exciter parameters for G2 were replaced with a gain of 200 and time constant of 0.02 s. This part describes the effects of K_{inert} variations on small-signal stability. The effects of K_{inert} were assessed under the performance of the proposed PSS, the parameters for which are listed in Table III. Details of the design procedure of the proposed PSS are provided in the following subsection. A three-phase fault was applied at Bus 5 at 5 s to observe the fast dynamic response to variations in K_{inert}, where K_{inert} was varied from 2 to 12 s to consider the plots of load angle of SG 2 δ_2 and active power output from the wind farm P_w, as shown in Fig. 10. The plots of δ_2 and P_w in Fig. 10 show significant disturbances due to the presence of system transients. Figure 10 clearly shows that a higher value of K_{inert} resulted in a greater amplitude of oscillation, which is not conducive to rotor-angle stability. By contrast, a smaller value of K_{inert} ensured better system performance.

TABLE III
PARAMETERS OF PROPOSED PSS AND CPSS FOR G2 OF MODIFIED IEEE 9-BUS TEST SYSTEM

Type of PSS	K_{pss}	T_w	T_1	T_2	T_3	T_4
Proposed PSS	254	10	0.1	0.01	0.2	0.02875
CPSS	127	10	0.1	0.01	0.2	0.21610

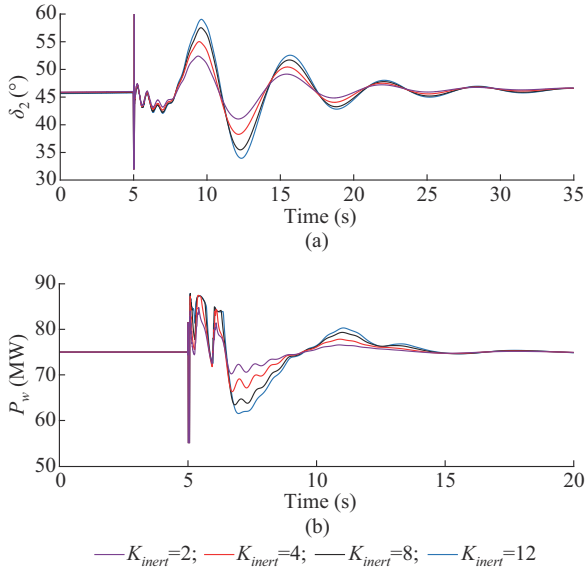

Fig. 10. Three-phase fault response of 9 bus system for variation of K_{inert}.

2) Effects of CPSS and Proposed PSS

The proposed PSS was designed according to the steps outlined in Algorithm 1 with $K_{inert}=4$ for the VIC of the DFIG. With the phase compensation technique described in Algorithm 1, the time constants of the proposed PSS obtained were $T_1=0.1$ s, $T_2=0.01$ s, $T_3=0.2$ s, and $T_4=0.02875$ s. According to the root locus plot in Fig. 11, the

critical gain was found to be $K_{pss}^{cr}=761$. Accordingly, K_{pss} was set to be $K_{pss}=K_{pss}^{cr}/3\approx 254$. The simulation results of post-fault response of the wind farm active power output P_w and load angle curve of G2 δ_2 were obtained for a three-phase fault applied at Bus 5, as shown in Fig. 12. It shows significant disturbances under the presence of system transients. Figure 12(a) and (b) clearly shows that the proposed PSS significantly outperformed the CPSS.

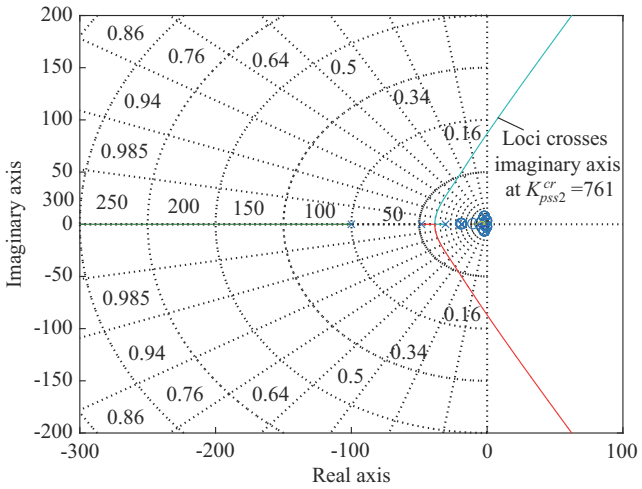

Fig. 11. Root locus of G2.

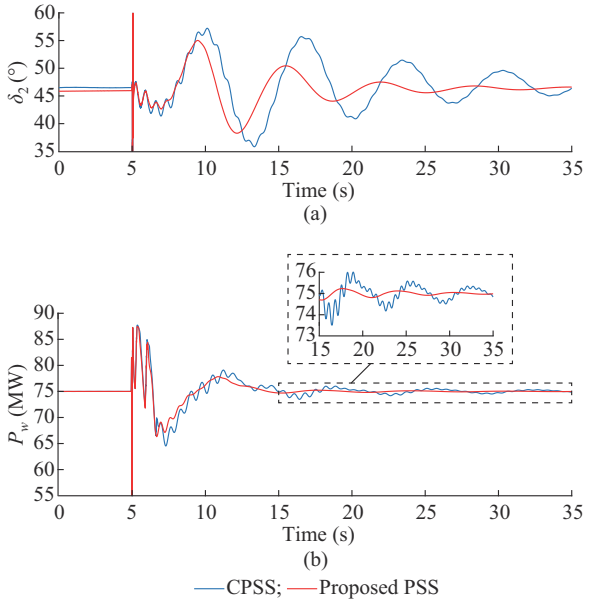

Fig. 12. Simulation result for 3-phase fault at bus 5 of 9-bus system. (a) δ_2. (b) P_w.

VII. Conclusion

Existing power sectors have recently witnessed rapid growth in terms of wind power integration. As wind power is intermittent, a common practice is to utilize VIC for frequency support. This paper investigated the dynamic effects of VIC and PLL on the small-signal stability of a power system. For this purpose, an average model of the DFIG-based wind farm was developed that incorporated VIC and PLL dynamics. An analytical formulation of damping and synchronizing coefficients was derived as functions of line reactance, K_{inert}, and PLL parameters. The significant coupling of the WES with the rest of the power system was observed with the incorporated VIC and PLL dynamics. This paper revealed to some extent the manner in which the gain of the inertial controller participated in power system stability by influencing the damping and synchronizing torque of the SG. The increase in value of virtual inertial gains K_{inert} reduced synchronizing torque but increased the damping torque of the system. Therefore, a system with high K_{inert} may lose synchronism. This paper also revealed that the proposed PSS tuning method improved the damping mechanism of power system over that of the CPSS. Thus, to improve the stability performance of a power system, the joint effects of the PLL and inertial controller of the DFIG must be considered in the design process of the PSS for the SG. The parameters of the proposed PSS were designed under a modified Heffron-Phillips model in a similar manner to that of the CPSS. However, more robustness could be obtained by applying some adaptive coordinated control methods. The parameters of the controllers were not optimized. Improved damping in the system could be achieved by considering advanced optimization techniques.

Appendix A

This section assists to derive ΔK_1-ΔK_6 discussed in Section II. From power balance equations (18) and (23), the following can be derived:

$$\begin{cases}\Delta\theta_p = T_1\Delta\delta + T_2\Delta E_q' \\ \Delta V_p = T_3\Delta E_q' + T_4\Delta\delta\end{cases} \tag{A1}$$

$$\begin{cases} T_1 = \dfrac{V_{p0}V_{n0}\cos\theta_{p0}/X_{L2}}{V_{P0}M_{en}/(X_{L2}X_1)+s^2K_{in}F_{pll}/(2\pi)} \\ T_2 = \dfrac{P_{g0}/E_{q0}'}{V_{P0}M_{en}/(X_{L2}X_1)+s^2K_{in}F_{pll}/(2\pi)} \\ T_3 = \dfrac{V_{p0}X_{L2}\cos(\delta_0-\theta_{p0})}{M_{en}} \\ T_4 = -\dfrac{P_{g0}X_1X_{L2}}{M_{en}} \end{cases} \tag{A2}$$

Substituting (A1) into (18), ΔP_g can be derived to the following form:

$$\Delta P_g = G_1(s)\Delta\delta + G_2(s)\Delta E_q' \tag{A3}$$

Further applying (A2) to the linearization of $\dot{E}_q'$ of synchronous generator mentioned in (14), the following can be derived:

$$\Delta\dot{E}_q' = -\frac{1}{T_{d0}'G_3(s)}\Delta E_q' - \frac{G_4(s)}{T_{d0}'}\Delta\delta + \frac{\Delta E_{fd}}{T_{d0}'} \tag{A4}$$

Based on (23), ΔV_t can be derived to:

$$\Delta V_t = G_5(s)\Delta\delta + G_6(s)\Delta E_q' \tag{A5}$$

Now $G_1(s)$-$G_6(s)$ can be separated as per the format expressed in (26) to derive ΔK_1-ΔK_6 of (25).

APPENDIX B

TABLE BI
PARAMETERS OF GENERATOR, AVR, AND TRANSFORMER

Equipment	Parameter	Value
Generator	H	6.4
	x_d	0.8958
	x'_d	0.1198
	x_q	0.8645
	T'_{d0}	6
AVR	K_a	400
	T_a	0.02
Transformer	x_T	0.0625

TABLE BII
PARAMETERS OF DFIG

Parameter	Value	Parameter	Value
Rating (MVA)	3.6	X_{sD} (p.u.)	3.37
H_D (s)	5.23	R_{rD} (p.u.)	0.005
R_{sD} (p.u.)	0.007	X_{rD} (p.u.)	3.47

REFERENCES

[1] P. H. A. Barra, W. C. de Carvalho, T. S. Menezes *et al.*, "A review on wind power smoothing using high-power energy storage systems," *Renewable & Sustainable Energy Reviews*, vol. 137, p. 110455, Mar. 2021.

[2] J. Slootweg and W. Kling, "The impact of large scale wind power generation on power system oscillations," *Electric Power Systems Research*, vol. 67, no. 1, pp. 9-20, Oct. 2003.

[3] W. Jin and Y. Lu, "Stability analysis and oscillation mechanism of the DFIG-based wind power system," *IEEE Access*, vol. 7, pp. 88937-88948, Jul. 2019.

[4] J. Liu, W. Yao, J. Wen *et al*., "Impact of power grid strength and PLL parameters on stability of grid-connected DFIG wind farm," *IEEE Transactions on Sustainable Energy*, vol. 11, no. 1, pp. 545-557, Jan. 2020.

[5] J. Ekanayake and N. Jenkins, "Comparison of the response of doubly fed and fixed-speed induction generator wind turbines to changes in network frequency," *IEEE Transactions on Energy Conversion*, vol. 19, no. 4, pp. 800-802, Dec. 2004.

[6] Z. Wang, C. Shen, and F. Liu, "Impact of DFIG with phase lock loop dynamics on power systems small signal stability," in *Proceedings of 2014 IEEE PES General Meeting*, Washington DC, USA, Oct. 2014, pp. 1-5.

[7] C. A. Martinez, X. Song, and M. Martha. (2010, Dec.). Review of the recent frequency performance of the eastern, western and ERCOT interconnections. [Online]. Available: https://gridintegration.lbl.gov/publications/review-recent-frequency-performance

[8] M. F. M. Arani and Y. A.-R. I. Mohamed, "Analysis and mitigation of undesirable impacts of implementing frequency support controllers in wind power generation," *IEEE Transactions on Energy Conversion,* vol. 31, no. 1, pp. 174-186, Mar. 2016.

[9] E. Rakhshani, A. Perilla, J. L. R. Torres *et al.*, "FAPI controller for frequency support in low-inertia power systems," *IEEE Open Access Journal of Power and Energy*, vol. 7, pp. 276-286, Jul. 2020.

[10] Y. Wang, J. Meng, X. Zhang *et al.*, "Control of PMSG-based wind turbines for system inertial response and power oscillation damping," *IEEE Transactions on Sustainable Energy*, vol. 6, no. 2, pp. 565-574, Apr. 2015.

[11] A. B. T. Attya and J. L. Dominguez-García, "Insights on the provision of frequency support by wind power and the impact on energy systems," *IEEE Transactions on Sustainable Energy*, vol. 9, no. 2, pp. 719-728, Apr. 2018.

[12] M. Garmroodi, D. J. Hill, G. Verbič *et al.*, "Impact of tie-line power on inter-area modes with increased penetration of wind power," *IEEE Transactions on Power Systems*, vol. 31, no. 4, pp. 3051-3059, Jul. 2016.

[13] E. Rakhshani, D. Gusain, V. Sewdien *et al.*, "A key performance indicator to assess the frequency stability of wind generation dominated power system," *IEEE Access*, vol. 7, pp. 130957-130969, Sept. 2019.

[14] A. Ashouri-Zadeh and M. Toulabi, "Adaptive virtual inertia controller for DFIGs considering nonlinear aerodynamic efficiency," *IEEE Transactions on Sustainable Energy*, vol. 12, no. 2, pp. 1060-1067, Apr. 2021.

[15] C. Zhong, J. Zhang, and Y. Zhou, "Adaptive virtual capacitor control for MTDC system with deloaded wind power plants," *IEEE Access*, vol. 8, pp. 190582-190595, Oct. 2020.

[16] M. Sun, Y. Min, L. Chen *et al.*, "Optimal auxiliary frequency control of wind turbine generators and coordination with synchronous generators," *CSEE Journal of Power and Energy Systems*, vol. 7, no. 1, pp. 78-85, Jan. 2021.

[17] A. A. Eshkaftaki, A. Rabiee, A. Kargar *et al.*, "An applicable method to improve transient and dynamic performance of power system equipped with DFIG-based wind turbines," *IEEE Transactions on Power Systems*, vol. 35, no. 3, pp. 2351-2361, May 2020.

[18] V. Gholamrezaie, M. G. Dozein, H. Monsef *et al.*, "An optimal frequency control method through a dynamic load frequency control (LFC) model incorporating wind farm," *IEEE Systems Journal*, vol. 12, no. 1, pp. 392-401, Mar. 2018.

[19] J. Ma, Y. Zhang, Y. Shen *et al.*, "Equipment-level locating of low frequency oscillating source in power system with DFIG integration based on dynamic energy flow," *IEEE Transactions on Power Systems*, vol. 35, no. 5, pp. 3433-3447, Sept. 2020.

[20] J. Ma, Y. Qiu, Y. Li *et al.*, "Research on the impact of DFIG virtual inertia control on power system small-signal stability considering the phase-locked loop," *IEEE Transactions on Power Systems*, vol. 32, no. 3, pp. 2094-2105, May 2017.

[21] S. Wang, J. Hu, X. Yuan *et al.*, "On inertial dynamics of virtual-synchronous-controlled DFIG-based wind turbines," *IEEE Transactions on Energy Conversion*, vol. 30, no. 4, pp. 1691-1702, Dec. 2015.

[22] M. A. P. Peter and W. Sauer, *Power System Dynamics and Stability*, Upper Saddle River: Prentice Hall, 1998.

[23] P. Kundur, M. Klein, G. J. Rogers *et al.*, "Application of power system stabilizers for enhancement of overall system stability," *IEEE Transactions on Power Systems*, vol. 4, no. 2, pp. 614-626, May 1989.

[24] D. Zhang, Y. Wang, J. Hu *et al.*, "Impacts of PLL on the DFIG-based WTG's electromechanical response under transient conditions: analysis and modeling," *CSEE Journal of Power and Energy Systems*, vol. 2, no. 2, pp. 30-39, Jun. 2016.

[25] E. V. Larsen and D. A. Swann, "Applying power system stabilizers part III: practical considerations," *IEEE Power Engineering Review*, vol. PER-1, no. 6, p. 63, Jun. 1981.

[26] E. V. Larsen and D. A. Swann, "Applying power system stabilizers part II: performance objectives and tuning concepts," *IEEE Power Engineering Review*, vol. PER-1, no. 6, p. 63, Jun. 1981.

[27] F. P. Demello and C. Concordia, "Concepts of synchronous machine stability as affected by excitation control," *IEEE Transactions on Power Apparatus and Systems*, vol. PAS-88, no. 4, pp. 316-329, Apr. 1969.

Balakrushna Sahu received the B.Tech. degree in electrical and electronics Engineering from the National Institute of Science and Technology, Berhampur, India, in 2010, and the M.E. degree from the National Institute of Technical Teachers' Training and Research, Bhopal, India, in 2014. He is currently pursuing the Ph.D. degree at the Department of Electrical Engineering, Indian Institute of Technology Ropar, Rupnagar, India. His current research interests include power system dynamics and stability of renewable integrated power system.

Bibhu Prasad Padhy received the B.E. degree from the University College of Engineering Burla, Burla, India, in 2006, the M.Tech. degree from the Indian Institute of Technology Roorkee, Roorkee, India, in 2009, and the Ph.D. degree from the Indian Institute of Technology Kanpur, Kanpur, India, in 2015, all in electrical engineering. He is currently an Assistant Professor with the Department of Electrical Engineering, Indian Institute of Technology Ropar, Rupnagar, India. His research interests include power system dynamics and stability, voltage-source-converter-based multi-terminal high-voltage direct current (HVDC) operation and control, renewable energy integration into power systems, wide-area controller design, power system optimization, and applications of artificial intelligence in power systems.